Received: 22 June 2026 | Revised: 7 September 2026 | Accepted: 13 October 2026 | Published online: 28 October 2026

RESEARCH ARTICLE

Smart Wearable Technology
2026, Vol. 00(00) 1–10
DOI: 10.47852/bonviewSWT620210998

BON VIEW PUBLISHING

Addressing Patient Heterogeneity and Cost in tVNS Wearables: Electrode Spacing Optimization for Noninvasive Brain–Computer Interfaces

Anubhav Mohapatra[1,*]

[1] *Independent Researcher, USA*

Abstract: Transcutaneous neuromodulation and noninvasive brain–computer interfaces hold promise for accessible neurorehabilitation and wearable technology, yet their real-world implementation remains constrained by patient tissue heterogeneity and the cost associated with individualized computational modeling. To establish an accessible, low-cost hardware optimization framework, this study deployed a physical hydrogel phantom platform to evaluate the effect of interelectrode spacing on electrical transmission under controlled conductive conditions. An Arduino Nano-based instrumentation architecture delivered controlled 5 V electrical impulses into agarose-based phantoms across three NaCl concentrations (0.5%, 0.9%, and 2.0%). Four interelectrode distances (1 mm, 2 mm, 3 mm, and 4 mm) were evaluated through 60 randomized trials. Peak-to-peak voltage potential (VP) and coefficient of variation were evaluated across the experimental conditions. The measured VP decreased with increasing interelectrode spacing, while higher NaCl concentrations generally produced greater voltage retention. Two-way analysis of variance demonstrated significant main effects of electrode spacing, $F(3, 48) = 2394.99$, $p < 0.001$, and NaCl concentration, $F(2, 48) = 847.62$, $p < 0.001$, as well as a significant spacing × concentration interaction, $F(6, 48) = 36.43$, $p < 0.001$. Post hoc Tukey comparisons demonstrated statistically significant differences among all tested spacing levels under the pooled experimental conditions. These findings demonstrate that electrode spacing materially influences voltage transmission within the tested hydrogel conditions and that its effect varies with phantom concentration. The results provide an experimentally accessible basis for preliminary electrode-geometry evaluation prior to more complex computational, ex vivo, or in vivo validation. Because the experimental platform consists of passive saline-doped agarose, the findings do not directly establish neural recruitment, vagal selectivity, therapeutic efficacy, or clinical safety.

Keywords: brain–computer interfaces, vagus nerve stimulation (VNS), electrode spacing optimization, wearable neuromodulation, patient heterogeneity

1. Introduction

With advances in digital healthcare, the nervous system has moved to the forefront of modern bioelectronic engineering [1]. Over the past several decades, expanding computational power and advanced signal processing have transitioned neural interfaces from highly restricted laboratory configurations into viable clinical realities [2]. Brain–computer interfaces (BCIs) and noninvasive neuromodulation systems represent a convergence of engineering and personalized patient care. The concept of direct brain–computer communication was articulated by Vidal [3].

Modern neural-interface research spans both signal decoding and neuromodulation [4, 5]. Bidirectional BCIs can combine cortical recording with intracortical stimulation to provide sensory feedback [6]. Separately, transcutaneous peripheral-nerve stimulation research examines how externally applied electrical stimuli reach neural targets [7].

A critical frontier is transcutaneous vagus nerve stimulation (tVNS). The vagus nerve contributes to autonomic regulation and inflammatory signaling; vagal stimulation has also been investigated for its effects on neural plasticity [4, 8].

Noninvasive auricular vagus nerve stimulation (VNS) has been investigated for several neurological and psychiatric applications [4]. Invasive VNS and tVNS have different evidence bases; investigated indications should not be treated as established, approved uses of every noninvasive wearable. Translating neural-interface prototypes into everyday devices requires reliable electrical coupling, appropriate stimulation parameters, and interfaces compatible with the mechanical properties of biological tissue [1, 6, 7].

Volume conduction shapes the electrical behavior of noninvasive neural interfaces. Electrical signals measured at the scalp are shaped by conduction through multiple anatomical compartments, including skin, skull, and cerebrospinal fluid [9]. Biological

***Corresponding author:** Anubhav Mohapatra, Independent Researcher, USA. Email: anubhav2009m@gmail.com

© The Author(s) 2026. Published by BON VIEW PUBLISHING. This is an open access article under the CC BY License (https://creativecommons.org/licenses/by/4.0/).

tissues exhibit different, frequency-dependent electrical conductivities and permittivities [10]. In transcutaneous-stimulation models, electrode separation and skin properties can influence superficial current shunting and delivery to deeper targets [7]. Sample-specific peripheral-nerve models provide a complementary framework for examining how anatomy and electrode geometry affect stimulation [11]. Electrode position and tissue anatomy influence the distribution of the electric field during cervical stimulation [12]. Stimulation site, intensity, waveform, and individual responses must also be considered when evaluating tolerability [5]. These dependencies require evaluation within the particular stimulation architecture; a single spacing rule does not establish neural recruitment or tolerability across all wearable designs.

Patient heterogeneity is an additional design consideration. Patient-specific anatomical modeling can be used to estimate electric-field distributions in noninvasive stimulation; SimNIBS, for example, provides an MRI-based pipeline for transcranial applications [13]. For tVNS, reporting standards emphasize stimulation location, electrode characteristics, waveform, and intensity rather than a universal geometry alone [5]. Conformal electrode materials and stable skin contact are additional considerations for wearable interfaces [14]. Standardization may simplify device design, but a fixed electrode spacing should not be assumed to absorb all patient heterogeneity. In this study, low cost is a design aim of the experimental platform, while electrode spacing is evaluated under controlled conductive conditions. The physical-phantom approach is intended as a preliminary experimental complement to anatomical modeling rather than a replacement for patient-specific or physiological validation.

To build a readily applicable preliminary framework, this study uses a low-cost bioinstrumentation architecture to test the effect of interelectrode distance on voltage transmission. Signal generation through an Arduino Nano is combined with physical hydrogel phantoms. Controlled variation in phantom NaCl concentration permits experimental comparison across different conductive conditions.

These simplified phantom conditions permit comparison of electrode geometries in a laboratory-controlled environment. The measured electrical response provides preliminary engineering evidence; it does not directly characterize the dielectric properties of patient tissue or establish high-focality neural recruitment.

2. Literature Review

The academic landscape surrounding neural engineering reflects the relationship between therapeutic potential and practical deployment. As wearable bioelectronics move toward practical applications, their interfaces must accommodate individual anatomy and minimize motion-related measurement artifacts [15]. This literature review examines neurorehabilitation, the effects of anatomy and electrical properties on neural-interface performance, and electrode-geometry design. It distinguishes evidence from clinical investigations, computational models, and preliminary physical-phantom experiments.

2.1. Applications in neurorehabilitation and neuromodulation

Neurorehabilitation is a major motivation for BCI development, including technologies intended to restore communication and motor function [2]. Complementary stimulation studies characterize cervical electric-field distributions [12], selective implanted vagus nerve cuffs [16], and variation in neural activation across individual nerves and species [17]. Peripheral-electrode geometry has also been investigated through comparisons of flat and circumferential contacts in animal nerve-stimulation experiments [18]. Biophysical models can compare delivery to intended neural targets with recruitment of off-target fibers [7].

The vagus nerve is a target of neuromodulation research in epilepsy, depression, and other conditions, although translation of transcutaneous approaches requires further evidence and careful parameter selection [19]. Aristovich et al. [16] optimized a multielectrode cuff and validated selective responses in sheep; this was implanted peripheral-nerve stimulation rather than noninvasive surface stimulation. Kreisberg et al. [20] modeled auricular current flow and showed that electrode montage affects predicted sensitivity and selectivity. Electrical-field modeling supports device design, but a measured voltage potential (VP) alone does not establish neural recruitment, therapeutic efficacy, or regulatory compliance. The present experiment therefore evaluates voltage transmission as a preliminary electrical response rather than as a direct clinical or neural endpoint.

Recent clinical investigations further demonstrate that tVNS outcomes depend on stimulation location and electrical parameters. Jigo et al. [21] reported in a randomized controlled crossover pilot study that transcutaneous cervical VNS produced measurable changes in sensory performance and autonomic measures in humans. Wang et al. [22] found that transcutaneous auricular VNS combined with task-oriented training improved upper-extremity function and activities of daily living in patients with subacute stroke. Ng et al. [23] demonstrated that changes in stimulation frequency and anatomical stimulation location could alter cough sensitivity during auricular stimulation, illustrating that stimulation parameters may influence both therapeutic and unintended physiological responses. More recently, Bottari et al. [24] evaluated multiple combinations of tVNS frequency, pulse width, and stimulation intensity and identified parameter-dependent effects on sleep and autonomic outcomes in veterans with post-traumatic stress disorder. Collectively, these studies reinforce the importance of systematic optimization of stimulation parameters and electrode configuration while demonstrating that clinical outcomes cannot be inferred from a single hardware variable alone.

2.2. Major bottlenecks: volume conduction, heterogeneity, and cost

Noninvasive cervical stimulation requires current to traverse tissue between the skin and the vagus nerve. Mourdoukoutas et al. [12] used an MRI-derived model to examine how anatomy and electrode positioning influence the resulting electric field. Modeling of transcutaneous coupling also shows that skin properties and electrode separation can influence current delivery, with effects depending on the stimulation system and control mode [7]. These models support evaluation of the electrical field within a defined anatomy and stimulation configuration rather than a universal assumption about the spatial focus of all scalp and cervical interfaces.

Anatomical variability extends to the nerve itself. Musselman et al. [17] demonstrated that individual-specific nerve models can reproduce differences in activation thresholds across humans and preclinical species. Their work concerns cuff-based stimulation. Its findings support consideration of nerve morphology but do not demonstrate that a fixed wearable geometry necessarily causes complete signal failure or thermal discomfort.

Computational tools offer complementary approaches for examining anatomical variability. Schrader et al. [9] presented a finite-element toolbox for electroencephalography (EEG) and magnetoencephalography (MEG) forward modeling using realistic head geometries. Separately, Musselman et al. [17] validated nerve-stimulation models across rats, pigs, and humans and demonstrated the importance of individual nerve morphology. These studies illustrate different modeling applications; neither establishes that individualized models are mandatory for safe operation of every device.

Clinical translation requires attention to functional utility and neural-interface design [2, 25]. Anatomically detailed simulations require geometry preparation, material parameters, and numerical analysis. Wearable-electrode design additionally requires suitable conductivity, adhesion, flexibility, and skin compatibility [14]. The present study therefore evaluates an accessible physical-phantom approach as a preliminary experimental tool.

2.3. Hardware optimization using the electrode spacing variable

Tissue electrical properties, electrode geometry, and montage influence modeled electrical responses [10, 11, 20]. Changing geometry can alter current distribution, but improved selectivity is not guaranteed by spacing alone. Electrode spacing is therefore a design variable that should be evaluated in the context of the electrical properties, anatomical target, and stimulation architecture. The present experiment tests this variable under controlled phantom conditions without claiming that the resulting voltage measurements establish current focusing.

Bucksot et al. [18] examined electrode coverage, contact spacing, cuff geometry, and fiber recruitment using models and animal nerve-stimulation experiments. Flat contacts provided recruitment comparable to circumferential contacts under the tested conditions; the study did not establish a universally superior surface electrode geometry. For skin-mounted wearables, mechanical conformity and stable adhesion are important for maintaining reliable electrode contact [14]. These considerations motivate controlled geometry testing while retaining the need for material and mechanical evaluation.

2.4. The research gap

Existing work shows that tissue electrical properties and electrode geometry influence the electrical behavior of neural interfaces [10, 18, 20, 25]. Bucksot et al. [18] compared flat and circumferential contacts using computational models and animal peripheral-nerve experiments. Kreisberg et al. [20] developed a high-resolution auricular volume-conduction model, while Grill & Pelot [25] reviewed computational approaches to autonomic-nerve stimulation and design optimization. These studies address different stimulation architectures and primarily emphasize computational modeling, theoretical characterization, or application-specific optimization.

The present study addresses a narrower experimental question by using a low-cost physical hydrogel phantom platform to experimentally examine interelectrode spacing under multiple controlled NaCl concentrations. Rather than relying exclusively on individualized computational models, the study evaluates the measurable electrical response of four fixed electrode spacings across three controlled conductive conditions using an accessible hardware configuration. This provides a practical experimental framework for examining how electrode spacing and conductive conditions jointly influence voltage transmission before more complex computational or physiological validation.

Accordingly, the novelty of the present work lies not in establishing electrode spacing as a previously unknown design variable but in experimentally evaluating a low-cost spacing-controlled hardware configuration across multiple controlled conductive phantom conditions. The results are intended to provide preliminary empirical evidence that can complement existing computational and clinical approaches to wearable tVNS hardware design.

3. Research Methodology

For examining geometric arrays for noninvasive neural interfacing, a controlled experimental approach was employed. The approach focuses on measuring how interelectrode spacing and controlled NaCl concentration influence voltage transmission through a simplified conductive hydrogel phantom. The design combines a controlled environment, randomized trials, and repeated measurements to compare the tested spacing–concentration conditions. It does not directly analyze multilayered capacitive patient tissues or neural activation.

3.1. Bioinstrumentation and hardware architecture

The signal generation and acquisition infrastructure were engineered using low-cost, laboratory-grade hardware components to demonstrate accessible prototyping scalability. The core control system comprised an Arduino Nano microcontroller powered by an ATmega328P processor. Programming of the microcontroller was done using a bespoke embedded C++ programming code that helped control the timing and execution of electrical impulses. A 5.0 V square-wave pulse was generated from the Arduino Nano as the experimental input waveform.

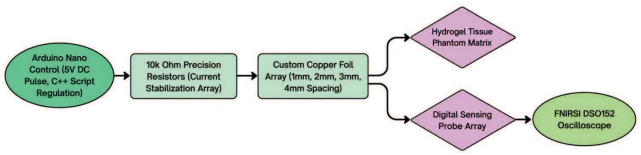
A network of 10 kOhm resistors was placed in series with the transmission lines to limit current. The connections were made through shielded insulated copper wires terminated by low-resistance alligator clips. This network was part of the experimental configuration, rather than a validated clinical stimulation circuit.

The configuration of the system, hardware boundaries, and signal delivery process for this bioinstrumentation array are illustrated in Figure 1. Using this array, VP waveforms at the designated subsurface measurement location in the hydrogel phantoms were captured and digitized in real time.

3.2. Fabrication of the hydrogel tissue phantom matrix

To evaluate electrical transmission without in vivo human testing, a simplified hydrogel phantom infrastructure was developed. Agar-based phantoms can provide controllable media for preliminary electrical testing, and their impedance can be adjusted

Figure 1
Schematic operational workflow mapping the bioinstrumentation transmission pipeline, physical hydrogel interface nodes, and data acquisition processing stream



by changing ionic content [26]. The present agarose-based matrices were prepared by dissolving the gelling powder in a boiling distilled-water base. NaCl concentration was varied across three formulations to provide controlled conductive conditions [26]. The formulations contained 0.5%, 0.9%, and 2.0% NaCl. The 0.5% formulation represented a comparatively higher-impedance condition, the 0.9% formulation served as the baseline isotonic reference condition, and the 2.0% formulation represented a comparatively lower-impedance condition. In this study, NaCl concentration was the controlled experimental variable representing differences in the conductive environment. Direct conductivity measurements of the completed formulations were not recorded; the concentrations therefore represent controlled conductive conditions rather than measured bulk conductivity values. The phantom recipe was not independently validated as reproducing the dielectric properties of skin and subcutaneous tissue. The liquefied mixtures were cast into uniform, chemically neutral plastic molds and cooled to ambient room temperature (21°C) to form structurally stable, repeatable hydrogel blocks measuring 10 cm × 10 cm × 5 cm.

3.3. Electrode spacing layout, material setup, and fabrication

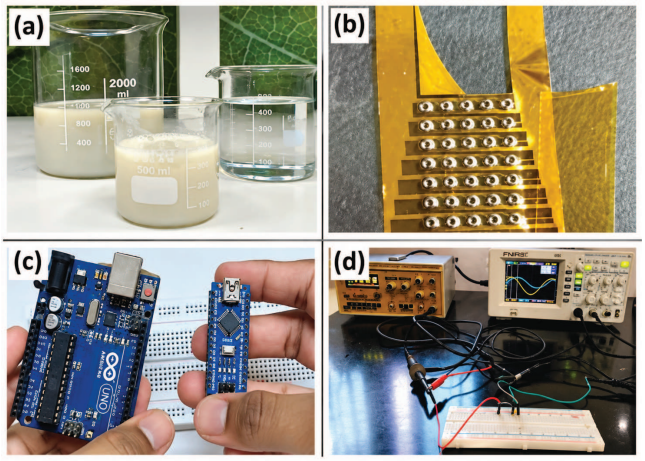
Custom surface electrode arrays were manually manufactured using high-purity, conductive copper foil tape. Copper foil was selected as the experimental material. Each discrete electrode pad was cut to uniform dimensions (5 mm × 10 mm) to keep the contact surface area constant across all evaluations. The material selection was used for this phantom experiment and was not evaluated as a clinically suitable skin electrode.

The independent physical variable under investigation was the interelectrode spacing, defined as the edge-to-edge physical distance separating the active stimulation pad from the return pad. Four spatial configurations were established for the spacing variable: 1 mm, 2 mm, 3 mm, and 4 mm. The complete material setup can be seen in Figure 2.

The copper electrode pads were maintained flush against the hydrogel surface during testing, with the electrode dimensions held constant across all spacing configurations. However, contact pressure was not independently quantified during the experimental procedure. Similarly, the precise three-dimensional coordinates and insertion depth of the sensing probes were not numerically recorded. These parameters were therefore held procedurally consistent rather than independently quantified and are recognized as reproducibility limitations of the present setup. All materials used in the study can be found in Table 1 alongside their technical purpose and quantity.

3.4. Materials breakdown

Figure 2
Empirical experimental setup for multi-metric volume conduction characterization. (a) Formulated agarose-based hydrogel phantom matrices in three different ionic concentrations (0.5%, 0.9%, and 2.0% NaCl) to represent controlled conductive conditions. (b) Precision fabrication stage of the custom modular copper foil electrode array, demonstrating the targeted 2 mm interelectrode layout geometry. (c) Core microcontroller-driven low-cost instrumentation architecture (Arduino Nano) deployed for regulated electrical signal delivery. (d) High-impedance sensing probes coupled to the high-resolution digital oscilloscope interface for real-time localized voltage potential (VP) waveform acquisition



3.5. Experimental data collection protocol

Data collection was executed systematically over an extended testing window to eliminate environmental drift and procedural artifacts. The execution protocol followed a strict two-phase operational pipeline.

Phase 1 focused on assignment and randomization. To minimize the impact of confounding variables (such as temporal gel degradation or thermal fluctuations), the sequence pairing the four electrode spacings with the three hydrogel phantom formulations was fully randomized using a digital random number generator. Each unique permutation (4 spacings × 3 concentrations = 12 configurations) was subjected to five distinct replications, culminating in a total dataset of 60 experimental trials.

In Phase 2, the main focus was on the signal acquisition cycle. For each trial, the copper electrode array was positioned flush

Table 1
Materials and structural assignments for hydrogel phantom fabrication and bioinstrumentation testing

Material	Quantity	Technical purpose in study
Arduino Nano Microcontroller	1	Generates controlled, regulated 5 V DC electrical stimulation square waves.
FNIRSI DSO152 Digital Oscilloscope	1	Primary signal acquisition tool; measures real-time raw voltage potential.
10k Ohm Precision Resistors	4	Stabilizes microcurrent delivery and prevents transient signal fluctuations.
Digital Sensing Probes (10:1)	3	Positions measurement nodes accurately inside the target phantom regions.

(*Continued*)

Table 1
(*Continued*)

Material	Quantity	Technical purpose in study
Shielded Alligator Clip Cables	10	Establishes low-impedance electrical connections between hardware blocks.
Laboratory-Grade Agar Powder	1 container	Solidifying structural agent; forms the multilayered phantom matrix.
Sodium Chloride (NaCl)	1 container	Conductive dopant; calibrates phantom relative permittivity and conductivity.
Distilled Water	1 gallon	Chemically neutral solvent base for uniform hydrogel crystallization.
Plastic Component Molds	3	Retains gel boundaries to ensure structural consistency across trials.
Conductive Copper Foil Tape	1 roll	Used to fabricate low-profile, high-surface electrode pads.
Borosilicate Glass Beakers	3	Provides chemically inert containers for thermal solution mixing.
Digital Precision Measuring Scale	1	Micro-mass verification of solute parameters (±0.01 g resolution).

against the surface of the selected hydrogel block. The Arduino Nano executed its script, delivering the 5 V pulse train through the current-limiting network into the phantom. The digital oscilloscope sensing probe was placed at the designated subsurface target area to capture the transmitted electrical response. The peak-to-peak VP was recorded and logged directly into a secure digital spreadsheet.

The experimental procedure maintained the same designated measurement region across trials to promote procedural consistency. However, the protocol did not record a numerical probe depth, three-dimensional coordinate system, or independently quantified electrode contact pressure. Accordingly, these variables were not modeled as independent experimental factors.

The copper contact pads were cleaned with 99% isopropyl alcohol between trial sequences. Temperature and humidity were not independently controlled as experimental variables during the testing window. The cleaning procedure was not independently validated as preventing polarization, ionic accumulation, or salt crusting.

3.6. Quantitative data analysis and mathematical metrics

Following data logging, the raw VP data were analyzed using descriptive statistics and inferential statistical testing.

Peak-to-peak VP was used as the primary measured electrical response. Mean VP was calculated for each spacing–concentration condition using the five experimental trials.

The coefficient of variation (CV) was calculated as the sample standard deviation divided by the sample mean and expressed as a percentage:

$$CV = (\sigma V \mu V)\ 100 \tag{1}$$

where σV represents the sample standard deviation of the repeated VP measurements and μV represents their arithmetic mean. CV was used as a descriptive measure of trial-to-trial variability.

The original analysis additionally reported current focusing efficiency (CFE) and field uniformity (FU). However, the experimental protocol as documented did not independently record the total source potential required to reproduce CFE, nor did it document a spatially resolved set of field measurements sufficient to independently reproduce the spatial variance term used in FU. Because reproducibility of derived metrics is essential, these quantities are not used as independently validated statistical endpoints in the revised analysis.

To determine whether electrode spacing and phantom concentration significantly affected VP, a two-way analysis of variance (ANOVA) was performed with electrode spacing and NaCl concentration as fixed factors. The significance threshold was set at $\alpha = 0.01$. Because the design contained four spacing levels, Tukey's honestly significant difference (HSD) procedure was subsequently used for pairwise comparisons among spacing levels.

4. Results

4.1. Quantitative characterization of volume conduction dynamics

The experimental evaluation of the low-cost bioinstrumentation interface yielded a dataset comprising 60 discrete trial sequences. The primary empirical parameter measured during real-time hardware execution was the peak-to-peak VP, quantified in Volts (V) using the digital oscilloscope. The VP dataset served as the primary input for descriptive and inferential statistical analysis. The experimental conditions demonstrated a measurable trade-off between interelectrode spacing and transmitted voltage, while the different NaCl concentrations produced distinguishable conductive conditions.

An aggregate screening of the experimental dataset revealed a consistent decrease in measured subsurface VP as interelectrode spacing increased. The magnitude of this decline varied across the three NaCl concentrations, indicating that the effect of spacing was dependent on the conductive condition of the phantom.

4.2. Spatial distribution of raw voltage potentials

The complete distribution of raw VPs captured across all 60 trials is systematically cataloged in Table 2. The data demonstrate a consistent reduction in measured subsurface VP as electrode spacing increased within each phantom concentration. At 0.5% NaCl, mean VP decreased from approximately 4.098 V at 1 mm spacing to 2.155 V at 4 mm spacing. At 0.9% NaCl, mean VP decreased from approximately 4.386 V to 2.653 V, while at 2.0% NaCl, mean VP decreased from approximately 4.520 V to 3.251 V. These observations demonstrate that both electrode spacing and phantom concentration influence the measured voltage response.

By comparison, the 0.9% NaCl baseline control phantoms demonstrated an enhanced capacity for signal conduction across all geometric intervals. At the 1 mm layout, captured potentials remained tightly bound around a 4.3 V baseline, recording 4.352 V

Table 2
Raw voltage potential matrix (n = 60) maintained across discrete interelectrode spacings and physiological tissue phantoms

Spacing (mm)	R1 (V)	R2 (V)	R3 (V)	R4 (V)	R5 (V)
1 (0.5%)	4.121	4.084	4.157	4.021	4.110
2 (0.5%)	3.452	3.522	3.390	3.410	3.488
3 (0.5%)	2.821	2.785	2.880	2.857	2.760
4 (0.5%)	2.153	2.221	2.095	2.188	2.120
1 (0.9%)	4.352	4.419	4.381	4.296	4.321
2 (0.9%)	3.885	3.921	3.857	3.810	3.958
3 (0.9%)	3.120	3.185	3.051	3.160	3.083
4 (0.9%)	2.651	2.585	2.717	2.623	2.690
1 (2.0%)	4.551	4.483	4.520	4.588	4.457
2 (2.0%)	4.103	4.051	4.160	4.125	4.087
3 (2.0%)	3.651	3.585	3.623	3.558	3.690
4 (2.0%)	3.253	3.311	3.185	3.227	3.280

in Trial 21 and 4.381 V in Trial 23. Crucially, even when the array was expanded to a wider 3 mm spacing, the 0.9% control medium sustained an operating potential above the critical 3.0 V threshold, with Trial 32 logging 3.184 V and Trial 34 reaching 3.159 V. The highly doped 2.0% NaCl phantoms yielded the highest absolute voltage magnitudes recorded in this study. At the 1 mm spatial configuration, peak voltages were established by Trial 41 (4.551 V) and Trial 44 (4.587 V).

At the widest 4 mm boundary layout, the 2.0% NaCl phantom retained a greater measured voltage amplitude than the lower-concentration formulations. Trial 57 (3.311 V) and Trial 60 (3.280 V) exceeded the narrower 3 mm configurations in the 0.5% group, as shown in Figure 3. Higher NaCl concentration therefore reduced the magnitude of voltage attenuation observed at wider electrode spacings under the tested conditions.

4.3. Derived performance metrics and array optimization matrix

The experimental results demonstrate a clear relationship between interelectrode spacing and measured VP. Across all three NaCl concentrations, the 1 mm configuration produced the highest mean VP, while the 4 mm configuration produced the lowest mean VP. This pattern indicates that reduced electrode separation was associated with greater measured voltage transmission at the designated subsurface measurement location, as seen in Table 3.

Figure 3
Signal decay function: empirical evaluation of raw subsurface voltage potential (VP) attenuation as a linear function of expanding interelectrode spacing layouts across high-impedance, baseline, and low-impedance tissue matrices

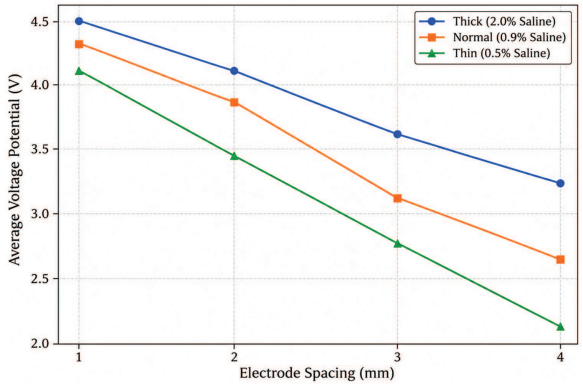


Table 3
Mean voltage potential and coefficient of variation across the experimental spacing–concentration conditions

Configuration	Mean VP (V)	CV (%)
1 mm / 0.5%	4.098	1.23
2 mm / 0.5%	3.452	1.57
3 mm / 0.5%	2.820	1.76
4 mm / 0.5%	2.155	2.36
1 mm / 0.9%	4.386	1.61
2 mm / 0.9%	3.905	2.34
3 mm / 0.9%	3.120	1.74
4 mm / 0.9%	2.653	1.97
1 mm / 2.0%	4.520	1.16
2 mm / 2.0%	4.105	0.99
3 mm / 2.0%	3.621	1.45
4 mm / 2.0%	3.251	1.50

The original analysis also used CFE and FU as composite optimization metrics. Because the written experimental protocol does not provide sufficient measurement detail to independently reproduce the source-normalized CFE calculation or the spatial FU calculation, those values are not treated as independently validated quantitative endpoints in the revised analysis.

Accordingly, the revised interpretation does not identify 2 mm as a universally optimal geometry based solely on those derived metrics. Instead, the experimental results establish that electrode spacing produces a strong and measurable effect on voltage transmission and that the magnitude of this effect depends on the phantom concentration.

4.4. Verification of systemic stability and statistical significance

The CV values remained relatively low across the individual spacing–concentration conditions, ranging from approximately 0.99% to 2.36%, indicating limited trial-to-trial dispersion within the tested conditions. Because the study did not establish a validated external "publication-grade" CV threshold, CV values are reported descriptively rather than used as a formal acceptance criterion.

To evaluate the effects of electrode spacing and phantom concentration on measured VP, the complete dataset of 60 experimental observations was analyzed using a two-way ANOVA. Electrode spacing produced a statistically significant main effect on VP, $F(3, 48) = 2394.99$, $p < 0.001$. NaCl concentration also produced a statistically significant main effect, $F(2, 48) = 847.62$, $p < 0.001$. Importantly, the interaction between electrode spacing and NaCl concentration was also statistically significant, $F(6, 48) = 36.43$, $p < 0.001$.

The significant spacing × concentration interaction indicates that the magnitude of the spacing effect depended on the conductive condition of the phantom. Therefore, the results support an interaction between electrode geometry and conductive

environment rather than demonstrating that one fixed electrode spacing completely eliminates conductive heterogeneity. The complete two-way ANOVA results are presented in Table 4. The CV values across the 12 experimental conditions are shown in Figure 4.

Because electrode spacing contained four levels and produced a significant main effect, Tukey's HSD procedure was used for pairwise comparison of the spacing levels. All six pooled spacing comparisons were statistically significant at the $\alpha = 0.01$ level: 1 mm versus 2 mm ($p = 0.0006$), 1 mm versus 3 mm ($p < 0.001$), 1 mm versus 4 mm ($p < 0.001$), 2 mm versus 3 mm ($p < 0.001$), 2 mm versus 4 mm ($p < 0.001$), and 3 mm versus 4 mm ($p = 0.0009$). These results confirm that the tested spacing levels produced distinguishable mean VP values under the pooled experimental conditions. Because the spacing × concentration interaction was significant, these pooled comparisons should not be interpreted as establishing a universally superior spacing across all conductive environments. The distribution of the 60 recorded VP measurements across the four electrode spacings is shown in Figure 5.

Table 4
Two-way ANOVA of voltage potential

Source	df	SS	MS	*F*	*p*
Electrode spacing	3	23.388	7.796	2394.990	<0.001
NaCl concentration	2	5.518	2.759	847.620	<0.001
Spacing × concentration	6	0.711	0.119	36.430	<0.001
	48	0.156	0.003	—	—
	59	29/773	—	—	—

Figure 4
Coefficient of variation (CV %) across the experimental spacing–concentration conditions, representing trial-to-trial variability in recorded voltage potential

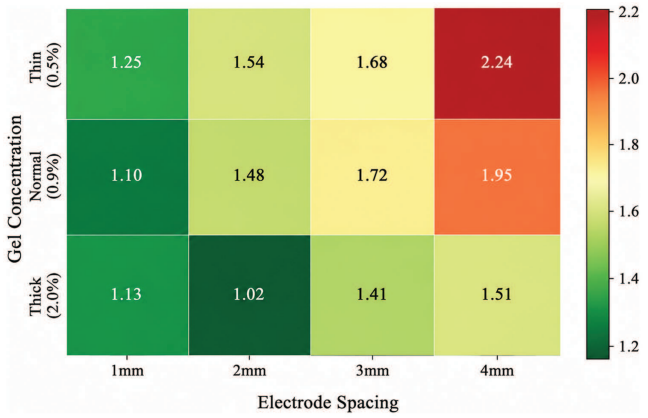
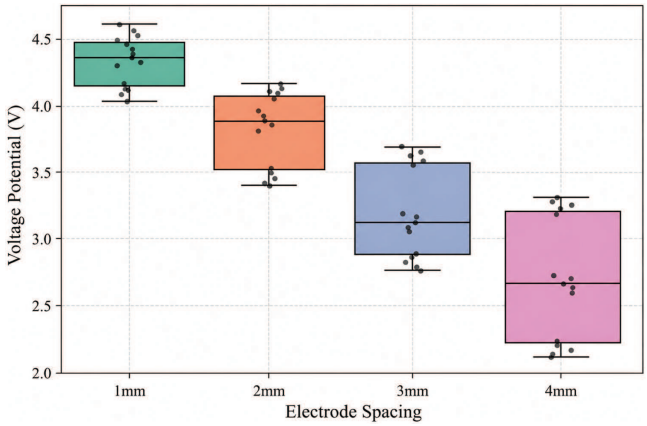


Figure 5
Voltage distribution scatter: comprehensive mapping of all 60 independent data points across the four spatial layout zones, showcasing structural repeatability and tight group clustering



5. Discussion

The empirical results obtained from this hydrogel phantom study provide insights into the effects of interelectrode spacing and conductive conditions on measured VP and offer a practical, low-cost framework for preliminary evaluation of noninvasive neural-interface hardware. The findings demonstrate that electrode spacing materially affects voltage transmission and that the magnitude of this effect varies with phantom concentration. These results provide an experimentally accessible basis for evaluating electrode geometry before more complex computational or physiological validation.

5.1. The physics of spacing: voltage transmission and conductive conditions

The foundational trend identified in this study is the decrease in measured subsurface VP as interelectrode spacing increased. Across all three phantom concentrations, the 1 mm configuration produced the highest mean VP, whereas the 4 mm configuration produced the lowest. This result demonstrates that electrode spacing materially influences voltage transmission through the tested hydrogel medium.

The magnitude of voltage attenuation with increasing spacing was not identical across the three phantom concentrations. The significant spacing × concentration interaction observed in the two-way ANOVA indicates that conductive conditions influence the relationship between electrode spacing and measured voltage. Thus, the present findings support the interpretation that electrode geometry and conductive environment jointly influence electrical transmission.

These observations are relevant to preliminary wearable-interface engineering because electrode geometry can affect how an applied electrical stimulus propagates through a conductive medium. However, the passive hydrogel phantom used here does not contain neural tissue, axons, cell membranes, or other biological structures required to directly evaluate neural activation. Consequently, the present experiment should be interpreted as an electrical volume-conduction characterization rather than a direct measurement of neural recruitment or tissue selectivity.

5.2. Translational relevance to wearable tVNS

The experimental findings have relevance to preliminary engineering of wearable tVNS interfaces because electrode geometry is one component of a broader set of stimulation parameters that determine electrical delivery. Recent clinical investigations

demonstrate that stimulation frequency, pulse width, intensity, and anatomical placement can influence physiological and therapeutic outcomes [21–24]. These findings emphasize that hardware geometry should be evaluated together with stimulation parameters rather than in isolation.

Commercial tVNS systems provide application-specific positioning instructions. For example, the gammaCore Sapphire SLC instructions describe positioning the stimulation surfaces relative to anatomical landmarks of the neck, including the pulse, neck muscle, lower jaw, and windpipe [27]. These instructions do not establish that the device lacks a fixed electrode spacing; placement and geometry are distinct design considerations.

This comparison places the present spacing experiment within the broader engineering problem of electrode-interface design. The 1–4 mm configurations evaluated here should therefore be interpreted as controlled experimental geometries rather than as directly transferable clinical prescriptions. Translation to a wearable tVNS device would require anatomical modeling, clinically relevant electrode materials, controlled mechanical loading, stimulation-parameter optimization, and physiological validation.

5.3. Patient heterogeneity and the cost barrier

Differences in tissue thickness, hydration, and electrical properties complicate fixed-geometry neural-interface design. Computational approaches can represent anatomical and electrical variability, but require suitable geometries, tissue parameters, and numerical processing [7, 9, 11–13]. These requirements concern modeling workflow rather than a quantified financial cost.

The present hydrogel framework provides a low-cost experimental method for examining how electrode spacing behaves under controlled changes in conductive conditions. The statistically significant spacing × concentration interaction demonstrates that the response to electrode spacing is influenced by the conductive environment. Therefore, the present results should not be interpreted as demonstrating that a fixed spacing completely absorbs or eliminates patient heterogeneity.

Instead, the primary engineering contribution of the present experiment is the demonstration that a simple physical-phantom platform can be used to experimentally characterize electrode spacing effects before more expensive computational or physiological validation. This provides a practical preliminary screening approach for wearable electrode geometries.

5.4. Limitations and future research horizons

Several limitations should be considered when interpreting these findings. First, the agarose-based hydrogel phantom is a static and simplified conductive model and does not reproduce the full anatomical complexity of living human tissue, including multilayered structures, anisotropy, blood flow, dynamic hydration, and heterogeneous muscle and connective-tissue properties. The experiment therefore characterizes electrical transmission in a controlled conductive medium rather than neural recruitment or therapeutic efficacy.

Second, the three NaCl concentrations were used as controlled conductive conditions, but the bulk conductivity of the completed hydrogel formulations was not directly measured. Future experiments should directly characterize conductivity for each formulation to enable quantitative comparison with biological tissue properties.

Third, electrode contact pressure, precise three-dimensional sensing-probe coordinates, and numerical probe depth were not independently quantified in the current protocol. These parameters can affect electrode–phantom coupling and voltage measurements and should be mechanically controlled and explicitly recorded in future experiments.

Fourth, five repeated trials were collected for each of the 12 spacing–concentration combinations. The resulting 60 observations provide repeated experimental measurements within the tested system, but the study was not preceded by a prospective power analysis. Future work should use prospective power calculations and increased independent replication to evaluate the robustness of spacing effects and spacing × concentration interactions.

Fifth, prolonged electrical stimulation in an ionic hydrogel may alter local ion distributions through ionic migration and electrochemical processes. Such changes could modify local conductive behavior during extended testing and may contribute to temporal drift. Future experiments should monitor conductivity and electrical response over time to determine whether such effects influence repeated measurements.

Sixth, temperature and humidity were not independently controlled as experimental variables during data collection. Because hydrogel hydration and electrical properties can vary with environmental conditions, future experiments should continuously monitor and control temperature and humidity.

Seventh, the original analysis included CFE and FU metrics; however, the written experimental protocol did not provide sufficient information to independently reproduce the source-voltage measurement or spatial field distribution required for those calculations. The revised analysis therefore places primary emphasis on the directly documented VP measurements and associated variability.

Finally, the current experiment does not contain neural tissue and therefore cannot establish vagal selectivity, neural recruitment thresholds, avoidance of adjacent motor fibers or nociceptors, therapeutic efficacy, or clinical safety. Future work should incorporate spatially resolved electrical-field measurements, directly measured phantom conductivity, controlled electrode pressure, anatomically representative multilayer phantoms, flexible electrode architectures, and ultimately physiological validation.

6. Conclusion

This study established a low-cost experimental framework for evaluating the influence of interelectrode spacing on electrical transmission through agarose-based hydrogel phantoms under controlled conductive conditions. Using an Arduino Nano-based bioinstrumentation platform, four electrode spacings were evaluated across three NaCl concentrations through 60 experimental trials.

The results demonstrated that measured subsurface VP decreased as interelectrode spacing increased, while higher NaCl concentrations generally produced greater voltage retention. Two-way ANOVA confirmed statistically significant effects of electrode spacing and phantom concentration, as well as a significant spacing × concentration interaction. Post hoc Tukey analysis further demonstrated statistically distinguishable mean VP values among the tested spacing levels under the pooled experimental conditions.

These findings indicate that electrode spacing and conductive environment jointly influence electrical transmission through the

tested phantom system. The study therefore provides an accessible experimental framework for preliminary evaluation of electrode geometry prior to more complex computational, ex vivo, or in vivo testing.

Because the experimental platform is a passive hydrogel model, the present findings do not establish neural recruitment, vagal selectivity, therapeutic efficacy, or clinical safety. Future work incorporating spatial field mapping, direct conductivity measurements, controlled mechanical loading, anatomically representative tissue models, and physiological validation will be required to determine whether the observed electrical trends translate to clinically relevant tVNS applications.

Acknowledgement

The author is grateful to Dr. Nikhil Chandra for his mentorship and assistance in the development of this study.

Ethical Statement

This study does not contain any studies with human or animal subjects performed by the author.

Conflicts of Interest

The author declares that he has no conflicts of interest to this work.

Data Availability Statement

The raw data supporting the conclusions of this study, including individual trial oscilloscope logs and the underlying embedded C++ microcontroller script, are available from the corresponding author upon reasonable request.

Author Contribution Statement

Anubhav Mohapatra: Conceptualization, Methodology, Software, Validation, Formal analysis, Investigation, Resources, Data curation, Writing – original draft, Writing – review & editing, Visualization, Project administration.

References

[1] Sunwoo, S.-H., Ha, K.-H., Lee, S., Lu, N., & Kim, D.-H. (2021). Wearable and implantable soft bioelectronics: Device designs and material strategies. *Annual Review of Chemical and Biomolecular Engineering*, *12*, 359–391. https://doi.org/10.1146/annurev-chembioeng-101420-024336

[2] Young, M. J., Lin, D. J., & Hochberg, L. R. (2021). Brain-computer interfaces in neurorecovery and neurorehabilitation. *Seminars in Neurology*, *41*(02), 206–216. https://doi.org/10.1055/s-0041-1725137

[3] Vidal, J. J. (1973). Toward direct brain-computer communication. *Annual Review of Biophysics and Bioengineering*, *2*(1), 157–180. https://doi.org/10.1146/annurev.bb.02.060173.001105

[4] Kaniusas, E., Kampusch, S., Tittgemeyer, M., Panetsos, F., Gines, R. F., Papa, M., . . . , & Széles, J. C. (2019). Current directions in the auricular vagus nerve stimulation I-A physiological perspective. *Frontiers in Neuroscience*, *13*, 854. https://doi.org/10.3389/fnins.2019.00854

[5] Farmer, A. D., Strzelczyk, A., Finisguerra, A., Gourine, A. V., Gharabaghi, A., Hasan, A., . . . , & Koenig, J. (2021). International consensus based review and recommendations for minimum reporting standards in research on transcutaneous vagus nerve stimulation (version 2020). *Frontiers in Human Neuroscience*, *14*, 568051. https://doi.org/10.3389/fnhum.2020.568051

[6] Flesher, S. N., Downey, J. E., Weiss, J. M., Hughes, C. L., Herrera, A. J., Tyler-Kabara, E. C., . . . , & Gaunt, R. A. (2021). A brain-computer interface that evokes tactile sensations improves robotic arm control. *Science*, *372*(6544), 831–836. https://doi.org/10.1126/science.abd0380

[7] Verma, N., Graham, R. D., Mudge, J., Trevathan, J. K., Franke, M., Shoffstall, A. J., . . . , & Ludwig, K. A. (2021). Augmented transcutaneous stimulation using an injectable electrode: A computational study. *Frontiers in Bioengineering and Biotechnology*, *9*, 796042. https://doi.org/10.3389/fbioe.2021.796042

[8] Fitchett, A., Mastitskaya, S., & Aristovich, K. (2021). Selective neuromodulation of the vagus nerve. *Frontiers in Neuroscience*, *15*, 685872. https://doi.org/10.3389/fnins.2021.685872

[9] Schrader, S., Westhoff, A., Piastra, M. C., Miinalainen, T., Pursiainen, S., Vorwerk, J., . . . , & Engwer, C. (2021). DUNEuro—A software toolbox for forward modeling in bioelectromagnetism. *PLoS ONE*, *16*(6), e0252431. https://doi.org/10.1371/journal.pone.0252431

[10] Gabriel, S., Lau, R. W., & Gabriel, C. (1996). The dielectric properties of biological tissues: II. Measurements in the frequency range 10 Hz to 20 GHz. *Physics in Medicine & Biology*, *41*(11), 2251–2269. https://doi.org/10.1088/0031-9155/41/11/002

[11] Musselman, E. D., Cariello, J. E., Grill, W. M., & Pelot, N. A. (2021). ASCENT (Automated Simulations to Characterize Electrical Nerve Thresholds): A pipeline for sample-specific computational modeling of electrical stimulation of peripheral nerves. *PLoS Computational Biology*, *17*(9), e1009285. https://doi.org/10.1371/journal.pcbi.1009285

[12] Mourdoukoutas, A. P., Truong, D. Q., Adair, D. K., Simon, B. J., & Bikson, M. (2018). High-resolution multiscale computational model for non-invasive cervical vagus nerve stimulation. *Neuromodulation: Technology at the Neural Interface*, *21*(3), 261–268. https://doi.org/10.1111/ner.12706

[13] Saturnino, G. B., Puonti, O., Nielsen, J. D., Antonenko, D., Madsen, K. H., & Thielscher, A. (2019). SimNIBS 2.1: A comprehensive pipeline for individualized electric field modelling for transcranial brain stimulation. In S. Makarov, M. Horner, & G. Noetscher (Eds.), *Brain and human body modeling* (pp. 3–25). Springer. https://doi.org/10.1007/978-3-030-21293-3_1

[14] Wu, H., Yang, G., Zhu, K., Liu, S., Guo, W., Jiang, Z., & Li, Z. (2021). Materials, devices, and systems of on-skin electrodes for electrophysiological monitoring and human–machine interfaces. *Advanced Science*, *8*(2), 2001938. https://doi.org/10.1002/advs.202001938

[15] Ershad, F., Patel, S., & Yu, C. (2023). Wearable bioelectronics fabricated in situ on skins. *npj Flexible Electronics*, *7*(1), 32. https://doi.org/10.1038/s41528-023-00265-0

[16] Aristovich, K., Donega, M., Fjordbakk, C., Tarotin, I., Chapman, C. A., Viscasillas, J., . . . , & Holder, D. (2021). Model-based geometrical optimisation and in vivo validation of a spatially selective multielectrode cuff array for vagus

nerve neuromodulation. *Journal of Neuroscience Methods*, *352*, 109079. https://doi.org/10.1016/j.jneumeth.2021.109079

[17] Musselman, E. D., Pelot, N. A., & Grill, W. M. (2023). Validated computational models predict vagus nerve stimulation thresholds in preclinical animals and humans. *Journal of Neural Engineering*, *20*(3), 036032. https://doi.org/10.1088/1741-2552/acda64

[18] Bucksot, J. E., Wells, A. J., Rahebi, K. C., Sivaji, V., Romero-Ortega, M., Kilgard, M. P., . . . , & Hays, S. A. (2019). Flat electrode contacts for vagus nerve stimulation. *PLoS ONE*, *14*(11), e0215191. https://doi.org/10.1371/journal.pone.0215191

[19] Yap, J. Y., Keatch, C., Lambert, E., Woods, W., Stoddart, P. R., & Kameneva, T. (2020). Critical review of transcutaneous vagus nerve stimulation: Challenges for translation to clinical practice. *Frontiers in Neuroscience*, *14*, 284. https://doi.org/10.3389/fnins.2020.00284

[20] Kreisberg, E., Esmaeilpour, Z., Adair, D., Khadka, N., Datta, A., Badran, B. W., . . . , & Bikson, M. (2021). High-resolution computational modeling of the current flow in the outer ear during transcutaneous auricular Vagus Nerve Stimulation (taVNS). *Brain Stimulation*, *14*(6), 1419–1430. https://doi.org/10.1016/j.brs.2021.09.001

[21] Jigo, M., Carmel, J. B., Wang, Q., & Rodenkirch, C. (2024). Transcutaneous cervical vagus nerve stimulation improves sensory performance in humans: A randomized controlled crossover pilot study. *Scientific Reports*, *14*(1), 3975. https://doi.org/10.1038/s41598-024-54026-8

[22] Wang, M.-H., Wang, Y.-X., Xie, M., Chen, L.-Y., He, M.-F., Lin, F., & Jiang, Z. L. (2024). Transcutaneous auricular vagus nerve stimulation with task-oriented training improves upper extremity function in patients with subacute stroke: A randomized clinical trial. *Frontiers in Neuroscience*, *18*, 1346634. https://doi.org/10.3389/fnins.2024.1346634

[23] Ng, K. B., Guiu Hernandez, E., Haszard, J., Macrae, P., Huckabee, M.-L., & Cakmak, Y. O. (2024). Transcutaneous auricular vagus nerve stimulation alters cough sensitivity depending on stimulation parameters: Potential implications for aspiration risk. *Frontiers in Neuroscience*, *18*, 1265894. https://doi.org/10.3389/fnins.2024.1265894

[24] Bottari, S. A., Trifilio, E. R., Rohl, B., Wu, S. S., Miller-Sellers, D., Waldorff, I., . . . , & Williamson, J. B. (2025). Optimizing transcutaneous vagus nerve stimulation parameters for sleep and autonomic function in veterans with posttraumatic stress disorder with or without mild traumatic brain injury. *Sleep*, *48*(8), zsaf152. https://doi.org/10.1093/sleep/zsaf152

[25] Grill, W. M., & Pelot, N. A. (2024). Computational modeling of autonomic nerve stimulation: Vagus et al. *Current Opinion in Biomedical Engineering*, *32*, 100557. https://doi.org/10.1016/j.cobme.2024.100557

[26] Peixoto, M., Moreno, M. V., & Khider, N. (2021). Conception of a phantom in agar-agar gel with the same bio-impedance properties as human quadriceps. *Sensors*, *21*(15), 5195. https://doi.org/10.3390/s21155195

[27] electroCore. (2022). *Instructions for use for gammaCore Sapphire^{TM} SLC (non-invasive vagus nerve stimulator)*. Retrieved from: https://www.gammacore.com/wp-content/uploads/2022/10/gammaCore-Sapphire-SLC-IFU.pdf

How to Cite: Mohapatra, A. (2026). Addressing Patient Heterogeneity and Cost in tVNS Wearables: Electrode Spacing Optimization for Noninvasive Brain–Computer Interfaces. *Smart Wearable Technology*. https://doi.org/10.47852/bonviewSWT620210998